

# RWKV-UNet: Improving UNet with Long-Range Cooperation for Effective Medical Image Segmentation

Juntao Jiang<sup>1\*</sup> Jiangning Zhang<sup>1,2\*</sup> Weixuan Liu<sup>3</sup> Muxuan Gao<sup>1</sup> Xiaobin Hu<sup>2</sup>  
Xiaoxiao Yan<sup>4</sup> Feiyue Huang<sup>4</sup> Yong Liu<sup>1†</sup>

<sup>1</sup>Zhejiang Univeristy <sup>2</sup>Youtu Lab, Tencent <sup>3</sup>Northeastern University <sup>4</sup>Ruijin Hospital

Code: <https://github.com/juntaoJianggavin/RWKV-UNet>

## Abstract

*In recent years, there have been significant advancements in deep learning for medical image analysis, especially with convolutional neural networks (CNNs) and transformer models. However, CNNs face limitations in capturing long-range dependencies while transformers suffer high computational complexities. To address this, we propose RWKV-UNet, a novel model that integrates the RWKV (Receptance Weighted Key Value) structure into the U-Net architecture. This integration enhances the model’s ability to capture long-range dependencies and improve contextual understanding, which is crucial for accurate medical image segmentation. We build a strong encoder with developed inverted residual RWKV (IR-RWKV) blocks combining CNNs and RWKVs. We also propose a Cross-Channel Mix (CCM) module to improve skip connections with multi-scale feature fusion, achieving global channel information integration. Experiments on benchmark datasets, including Synapse, ACDC, BUSI, CVC-ClinicDB, CVC-ColonDB, Kvasir-SEG, ISIC 2017 and GLAS show that the RWKV-UNet achieves state-of-the-art performance on various types of medical image segmentation. Additionally, smaller variants, RWKV-UNet-S and RWKV-UNet-T, balance accuracy and computational efficiency, making them suitable for broader clinical applications.*

## 1. Introduction

Computer-aided medical image analysis plays a crucial role in modern healthcare. Automated image segmentation is a critical component of this process, as it divides complex images into distinct regions, allowing specific tissues, organs, or lesions to be more clearly visible, improving diagnostic accuracy, and facilitating the development of personalized treatment plans. The rise of deep learning [28] has greatly advanced image segmentation by automatically learning intricate patterns within images with deep neural networks,

improving the precision and efficiency of the analysis.

Current medical image segmentation approaches mainly rely on fully convolutional neural networks (FCNs) characterized by a U-shaped architecture. U-Net [46] is specifically designed for image segmentation tasks, particularly in the medical imaging domain. Its distinctive features include an encoder-decoder structure that enables effective downsampling and upsampling of images, along with skip connections. This design allows U-Net to capture both high-level semantic features and fine-grained details, resulting in improved segmentation accuracy. The architecture’s success has led to the development of numerous variants, such as Attention U-Net [40], U-Net++[61], U-Net3+ [22], which have further enhanced its performance and expanded its applicability.

While CNNs excel at capturing local features through fixed-size kernels, they often struggle with long-range dependencies needed for understanding complex structures. Transformers, with their self-attention mechanism, capture global context and intricate patterns across entire images. Combining these architectures allows U-Net to retain fine detail, as seen in models like TransUNet [9], MT-UNet [53], and HiFormer[21]. However, transformers have  $O(N^2)$  complexity in self-attention, which makes them computationally intensive for high-resolution scans. The trade-off between accuracy and efficiency is important in clinical scenarios, thus reducing computational complexity without significantly compromising accuracy is highly desirable.

Recently, sequence modeling methods based on linear attention mechanisms, such as Mamba [17] and RWKV [41], have attracted significant attention and been applied to computer vision [16, 62] and medical image segmentation tasks [33, 38, 47]. These models excel at capturing long-range dependencies with high accuracy, effectively preserving important contextual information across extensive image regions. In addition, their linear computational complexity greatly improves efficiency, making them suitable for large-scale or high-resolution images while reducing processing demands.

Inspired by Vision-RWKV [47], we propose a novel RWKV-UNet, integrating convolutional layers with the spatial mix for medical image segmentation. The motivation behind this design is to take advantage of RWKV’s ability to capture long-range dependencies and combine it with the strengths of convolution localization, in order to achieve more precise and context-sensitive segmentation results. To evaluate our model’s effectiveness, we conducted experiments on benchmark datasets including Synapse [27], ACDC [5], BUSI [1], CVC-ClinicDB [4], CVC-ColonDB [3], Kvasir-SEG [25], ISIC 2017 [13] and GLAS [49], where it achieves state-of-the-art (SOTA) performance, highlighting its potential as a robust tool for medical image analysis.

In summary, our contributions are threefold.

- We propose a novel U-Net architecture based on a combination of RWKV and convolutional layers. An encoder based on the inverted residual RWKV (IR-RWKV) module is designed, effectively combining global and local information, with enhanced feature extraction capabilities through pre-training.
- A Cross-Channel Mix module is designed to improve the skip connections in U-Net, facilitating multi-scale information fusion and enhancing the model’s feature representation across different scales.
- Experiments conducted on datasets of different modalities show that the model achieves SOTA performance, demonstrating strong segmentation capabilities. We also propose relatively smaller models, RWKV-UNet-S and RWKV-UNet-T, which strike a balance between performance and computational efficiency, making them suitable for a wider range of scenarios.

## 2. Related Work

### 2.1. UNet Variants

U-Net is a deep learning architecture designed for image segmentation, originally developed for biomedical images. Its symmetrical U-shaped structure consists of an encoder and a decoder, where the encoder progressively extracts features and reduces spatial dimensions, while the decoder gradually restores spatial information and generates high-resolution outputs. Skip connections are used to combine feature maps from the encoder layers with those from the decoder layers, ensuring the preservation of details. Variations in U-Net improve its performance through various means, including the use of deeper encoders such as ResNet [59], the introduction of gating mechanisms to focus on important features [40], improvements in skip connection formats [22, 42, 61, 64] to recover more spatial details, as well as adaptations for 3D images [12, 39]. Some studies have explored combining MLP/KAN with UNet to achieve long-range dependencies [30, 35, 50]. These improvements al-

low U-Net to demonstrate higher accuracy and adaptability in various image segmentation tasks.

**Attention-based Improvements.** Attention-based U-Net has several advantages, primarily its ability to capture global context information, which enhances the model’s understanding of long-range dependencies. Furthermore, the self-attention mechanism of Transformers allows the model to focus more effectively on key information. Variants of attention-based U-Net include pure Transformer models [2, 8, 19, 23], which rely entirely on self-attention mechanisms for feature extraction and image segmentation. Another category consists of hybrid architectures that combine Transformers with CNNs [7, 9, 21, 26, 52, 53, 55, 57], which leverage the local feature extraction capabilities of CNNs along with the global information processing strengths of Transformers to better capture image details and structural information. Recently, Mamba [17]’s success in NLP and vision tasks [62] has drawn significant attention to SSM, which can be considered a form of linear attention. SSM-based UNet variants [33, 34, 38, 47, 54] capture long-range dependencies effectively and offer linear computational complexity, enhancing accuracy and efficiency in image segmentation tasks.

### 2.2. Receptance Weighted Key Value (RWKV)

Receptance Weighted Key Value (RWKV) [41] was initially developed for natural language processing tasks. It combines the linear complexity of RNNs with the parallel processing advantages of Transformers, resulting in excellent performance, constant memory usage, and consistent inference generation speed. Building on this, Vision-RWKV (VRWKV) [16] introduces RWKV to computer vision tasks, achieving success in image classification, object detection, and semantic segmentation. It efficiently handles sparse inputs and robust global processing and allows for high-resolution image processing without the need for window operations. Related efforts have also emerged in medical image analysis tasks. Restore-RWKV [56] is an RWKV-based model for medical image restoration, enhancing the efficiency and effectiveness of medical image restoration through the introduction of the linear complexity Re-WKV attention mechanism and the omnidirectional token shift (Omni-Shift) layer. BSBP-RWKV [60, 60] achieves superior accuracy in medical image segmentation by combining the noise reduction advantages of Perona-Malik diffusion with the efficient RWKV structure.

## 3. Methodology: RWKV-UNet

### 3.1. Overall Architecture

The overall architecture of the proposed RWKV-UNet is presented in Figure 1. RWKV-UNet consists of an encoder,

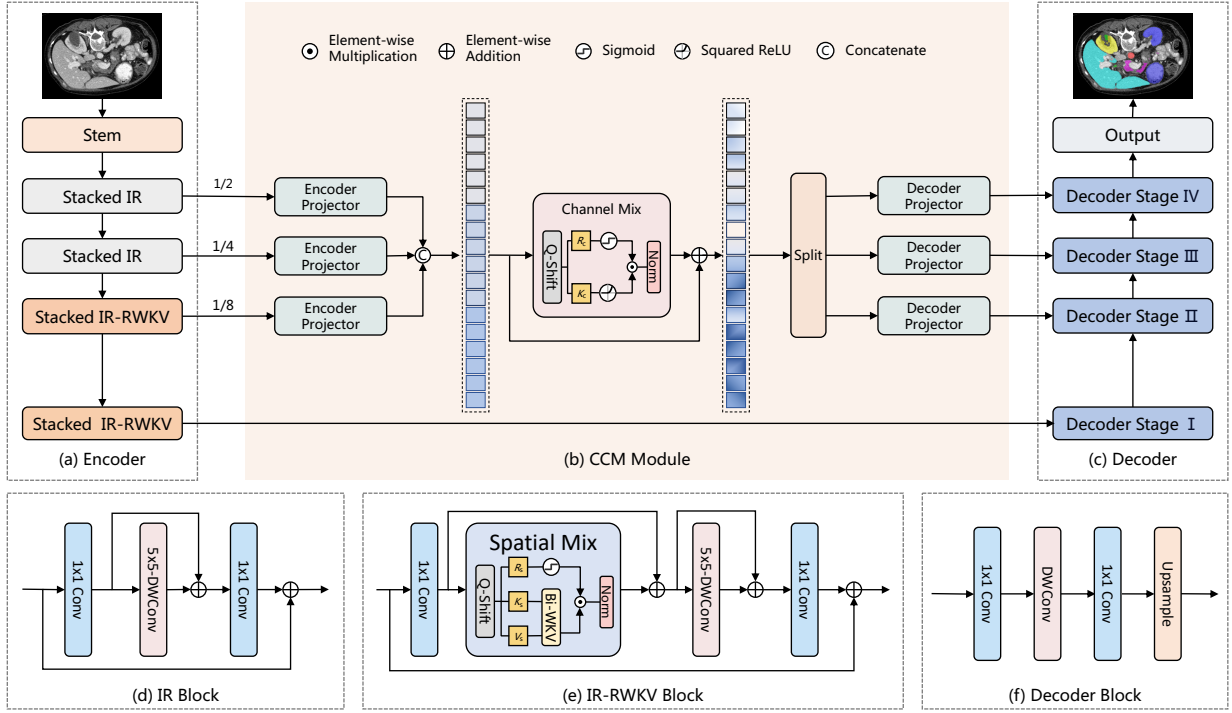


Figure 1. **Overall architecture of the proposed RWKV-UNet.** (a) the encoder constructed by stacked IR blocks and stacked IR-RWKV blocks, (b) Cross-Channel Mix (CCM) Module, (c) the decoder constructed by point convolution layers and depthwise convolution layers, (d) the Inverted Residual (IR) block, (e) the Inverted Residual RWKV (IR-RWKV) block, (f) the architecture of the decoder block, containing a point-convolution layer and a  $9 \times 9$  DW-Conv layer, following a point operation layer and an upsampling operation.

a decoder and skip connections with a Cross-Channel Mix (CCM) Module.

### 3.2. Effective Encoder in RWKV-UNet

**Inverted Residual RWKV (IR-RWKV) Block.** We employ the spatial-mix module in Vision RWKV and Depth-Wise Convolution (DW-Conv) with a skip connection to combine global and local dependency, and trade-off model cost and accuracy. The process of expanding and reducing dimensions enhances feature representation by capturing richer details while preventing information bottlenecks. Given a feature map  $X \in \mathbb{R}^{C_{in} \times H \times W}$ , the processing flow through the IR-RWKV module is as follows:

Normalize and project the input  $X$  to an intermediate dimension  $C_{mid}$  using a  $1 \times 1$  Convolution layer:

$$I_1 = \text{LayerNorm}(\text{Conv}_{1 \times 1}(X)), \quad (1)$$

where  $I_1 \in \mathbb{R}^{C_{mid} \times H \times W}$ .  $C_{mid}$  should be greater than  $C_{in}$  to achieve dimension expansion.

Divide the feature map into patches of size  $1 \times 1$ . Then the Spatial Mix in VRWKV is applied:

$$I_2 = \text{Unfolding}(I_1), \quad (2)$$

$$I_3 = \text{SpatialMix}(\text{LayerNorm}(I_2)) + I_2, \quad (3)$$

where  $I_2 \in \mathbb{R}^{C_{mid} \times N}$ ,  $I_3 \in \mathbb{R}^{C_{mid} \times N}$ .

Convert the feature sequence back into a 2D feature map  $I_4 = \text{Folding}(I_3) \in \mathbb{R}^{C_{mid} \times H \times W}$ , and use a  $5 \times 5$  DW-Conv layer for local feature aggregation:

$$I_5 = \text{DW-Conv}(I_4) + I_4, \quad (4)$$

where  $I_5 \in \mathbb{R}^{C_{mid} \times H' \times W'}$ .  $H' \times W'$  is determined by the stride of DW-Conv.

Finally, project  $I_5$  to the output dimension and add a global skip connection:

$$F = \text{Conv}_{1 \times 1}(I_5) + X, \quad (5)$$

where  $F \in \mathbb{R}^{C_{out} \times H' \times W'}$ .

**Inverted Residual (IR) Block.** An IR block contains a point convolution layer, a DW-Conv layer and a point convolution layer with local and global residual skips, removing the spatial mix as well as the unfolding and folding processes from the IR-RWKV.

Table 1. RWKV-UNet Encoder Configurations Across Stages

Stage	Parameter	Enc-T	Enc-S	Enc-B
<b>Stem</b>	Dimension	24	24	24
<b>Stage I</b>	Depth	2	3	3
	Dimension	32	32	48
	Expansion	2.0	2.0	2.0
	Spatial Mix	✗	✗	✗
<b>Stage II</b>	Depth	2	3	3
	Dimension	48	64	72
	Expansion	2.5	2.5	2.5
	Spatial Mix	✗	✗	✗
<b>Stage III</b>	Depth	4	6	6
	Dimension	96	128	144
	Expansion	3.0	3.0	4.0
	Spatial Mix	✓	✓	✓
<b>Stage IV</b>	Depth	2	3	3
	Dimension	160	192	240
	Expansion	3.5	4.0	4.0
	Spatial Mix	✓	✓	✓
<b>Parameters</b>		2.6M	9.4M	16.7M
<b>FLOPs</b>		1.9G	4.8G	9.0G

### Effective Encoder with Stacked IRs and IR-RWKVs.

We construct the RWKV-UNet encoder by stacking the IR and IR-RWKV blocks. The encoder comprises a stem stage followed by four stages. The first blocks in stages I, II, III and IV do not have residual connections and use a DW-Conv with a stride of 2 to achieve downsampling. After the first block, Stages I and II are composed of stacked IR blocks without Spatial Mix. In Stages III and IV, a series of IR-RWKV blocks follow the first block.

**Scale Up.** As shown in Table 1, we implement three different sizes of encoders with different numbers of IR and IR-RWKV blocks in each stage (depths), different embedding dimensions and expansion ratios for  $C_{\text{mid}}$ : Encoder-Tiny (Enc-T), Encoder-Small (Enc-S), and Encoder-Base (Enc-B), allowing flexibility to scale up the model according to different resource constraints and application needs.

**Pre-training Manner.** We pre-train the encoders of different sizes on ImageNet-1K [14] with a batch size of 1024 for 300 epochs using the AdamW [36] optimizer. These pre-trained weights of different sizes will be used in medical segmentation tasks, enabling improved feature extraction and faster convergence.

**Comparison with other attention types** We conduct experiments by replacing the spatial mix in the encoder of RWKV-UNet with other attention mechanisms, such as self-attention [51], focused linear attention [18] and Bi-Mamba used in Vision Mamba [62], as well as by removing this

Table 2. Comparison results of models with different attention mechanisms on Synapse dataset.

Attention Type	Average		FLOPs
	HD95 ↓	DSC ↑	
No Attention	18.06	77.05	4.55G
Multi-Head Self-attention [51]	16.95	77.60	14.89G
Focused Linear Attention [18]	18.45	75.86	11.69G
Bi-Mamba [62]	<b>13.13</b>	<b>77.86</b>	14.53G
Spatial-Mix [47]	<u>14.03</u>	<b>78.68</b>	11.22G

module entirely. The total training epochs are 60. The results shown in Table 2 indicate that the model with Spatial-Mix achieves the best DSC with the lowest computational cost compared to other attention mechanisms, showcasing its efficiency and effectiveness. And all kinds of attention mechanisms can lead to improvement compared to pure CNN structure except focused linear attention.

### 3.3. Decoder Design

We design our CNN-based decoder block with a point-convolution layer and a  $9 \times 9$  DW-Conv layer, following a point operation layer and an upsampling operation. Consider the input feature map  $X \in \mathbb{R}^{C_{\text{in}} \times H \times W}$ ; in depthwise convolution, the number of input channels is  $C_{\text{in}}$ , and the second point convolution maps the  $C_{\text{in}}$  channels to  $C_{\text{out}}$ . The computational complexity of a standard convolution is:

$$H \times W \times C_{\text{in}} \times (C_{\text{out}} \times K^2). \quad (6)$$

The computational complexity of pointwise convolution + depthwise convolution + pointwise convolution is:

$$H \times W \times C_{\text{in}} \times (C_{\text{in}} + K^2 + C_{\text{out}}), \quad (7)$$

where  $K$  is the kernel size. The latter method is more computationally efficient for the use of larger kernels, as the complexity is proportional to  $C_{\text{in}} \times K^2$  rather than  $C_{\text{in}} \times C_{\text{out}} \times K^2$ .

### 3.4. Cross-Channel Mix for Multi-scale Fusion

Inspired by the Channel Mix in VRWKV, we propose Cross-Channel Mix (CCM), a module that can effectively extract channel information across multi-scale encoder features. By capturing the rich global context along channels, CCM further enhances the extraction of long-range contextual information.

Define output feature map of Stage I, Stage II and Stage III of the designed encoder are  $F_1$ ,  $F_2$ , and  $F_3$ , which has different spatial dimensions and channel counts:  $F_1 \in \mathbb{R}^{C_1 \times H_1 \times W_1}$ ,  $F_2 \in \mathbb{R}^{C_2 \times H_2 \times W_2}$ ,  $F_3 \in \mathbb{R}^{C_3 \times H_3 \times W_3}$ . ( $H_1 > H_2 > H_3$ ,  $W_1 > W_2 > W_3$  and  $C_3 > C_2 > C_1$ ).

We reshape and map smaller features to match the largest

feature’s size and dimension:

$$\begin{aligned}\tilde{F}_i &= \text{Conv}_{C_i}(\text{Upsample}(F_i)), \quad i = 2, 3 \\ \tilde{F}_1 &= \text{Conv}_{C_1}(F_1),\end{aligned}\quad (8)$$

where  $\tilde{F}_1 \in \mathbb{R}^{C_1 \times H_1 \times W_1}$ ,  $\tilde{F}_2 \in \mathbb{R}^{C_1 \times H_1 \times W_1}$ , and  $F_3 \in \mathbb{R}^{C_1 \times H_1 \times W_1}$ .

We concatenate the adjusted feature maps along the channel dimension to produce a combined feature map:

$$F_{\text{cat}} = \text{Concat}(\tilde{F}_1, \tilde{F}_2, \tilde{F}_3), \quad (9)$$

where  $F_{\text{cat}} \in \mathbb{R}^{3C_1 \times H_1 \times W_1}$ .

Divide the feature map into patches:  $F_{\text{unf}} = \text{Unfolding}(F_{\text{cat}}) \in \mathbb{R}^{3C_1 \times N}$ . Then apply the Channel Mix in VRWKV, performing multi-scale global feature fusion in the channel dimension:

$$F_{\text{mix}} = \text{ChannelMix}(\text{LayerNorm}(F_{\text{unf}})) + F_{\text{unf}}, \quad (10)$$

where  $F_{\text{mix}} \in \mathbb{R}^{3C_1 \times N_1}$ . Project it back to 2D feature,  $F_{\text{fold}} = \text{Folding}(F_{\text{mix}}) \in \mathbb{R}^{3C_1 \times H_1 \times W_1}$ , and  $N_1 = H_1 \times W_1$ .

The folded feature map  $F_{\text{fold}}$  is split back into three separate features:  $[F_{\text{fold}}^{(1)}, F_{\text{fold}}^{(2)}, F_{\text{fold}}^{(3)}]$ . Each split feature undergoes a reshape operation and a convolution to restore its original sizes and dimensions:

$$F'_i = \text{Conv}_{C_i}(\text{Reshape}(F_{\text{fold}}^{(i)})), \quad i = 1, 2, 3 \quad (11)$$

where  $F'_1 \in \mathbb{R}^{C_1 \times H_1 \times W_1}$ ,  $F'_2 \in \mathbb{R}^{C_2 \times H_2 \times W_2}$  and  $F'_3 \in \mathbb{R}^{C_3 \times H_3 \times W_3}$ .  $F'_1, F'_2$  and  $F'_3$  will be concatenated with the output of the decoder Stage III, Stage II and Stage I.

## 4. Experiments

### 4.1. Experimental Setup

**Datasets and Metrics.** Experiments are conducted on Synapse [27] for multi-organ Segmentation in CT images, ACDC [5] for cardiac segmentation in MRI images, BUSI [1] for breast tumor segmentation in ultrasound images, CVC-ClinicDB [4], CVC-ColonDB [3], Kvasir-SEG [25] for poly segmentation, ISIC 2017 [13] for skin lesion segmentation and GLAS [49] for gland segmentation. The average Dice Similarity Coefficient (DSC) and average 95% Hausdorff Distance (HD95) are used as evaluation metrics. Specific details for datasets can be seen in Appendix.

**Comparison Methods.** We use U-Net [46], R50 U-Net [20, 46], R50 Att-Unet [20, 40], ViT [15] + CUP [9], R50-ViT [15, 20] + CUP [9], TransUNet [9], Swin-UNet [6], TransClaw U-Net [7], MT-UNet [53], UC-TransNet [52], MISSFormer [23], CASTformer [57],

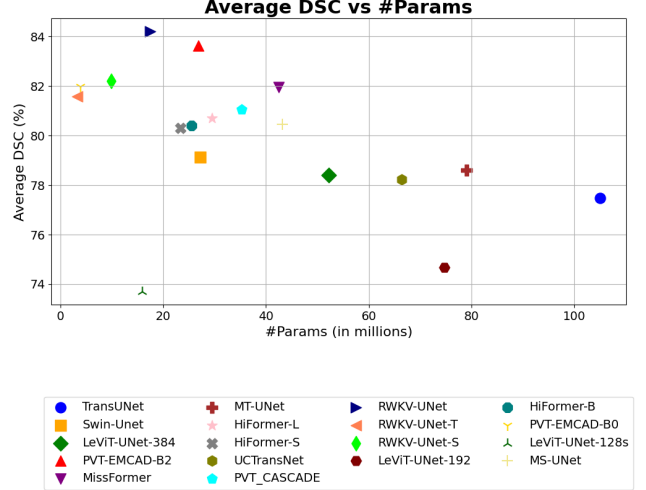


Figure 2. Average DSC vs. #Params for different methods on Synapse multi-organ segmentation dataset.

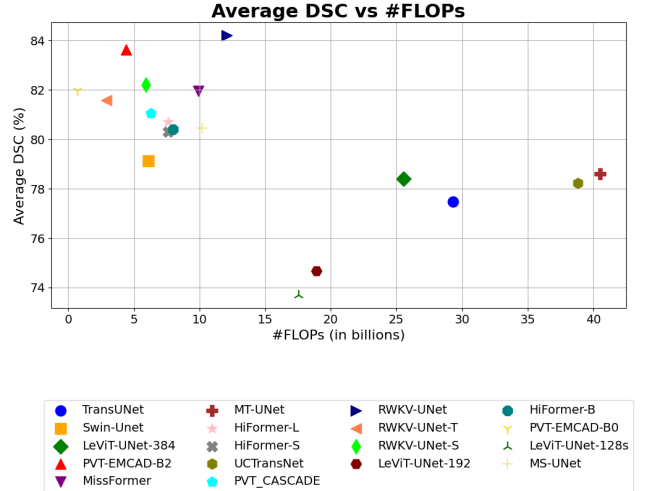


Figure 3. Average DSC vs. #FLOPs for different methods on Synapse multi-organ segmentation dataset.

TransDeepLab [2], CTC-Net [58], MS-UNet [8], LeViT-UNet-384 [55], HiFormer-L [21], PVT-CASCADE [44], TransCASCADE [44], AiA-UNet [43], MetaSeg-B [26], VM-UNet [47], PVT-EMCAD-B2 [45], SelfReg-UNet [46, 63], SelfReg-SwinUnet [6, 63], FCBFormer [48], Rolling-UNet-M [31], U-KAN [30] as baselines.

**Implementation Details.** All experiments are all performed on PG500-216(V-100) with 32 GB memory. The resolution of the input images is resized to  $224 \times 224$  for Synapse and ACDC, and  $256 \times 256$  for binary segmentation tasks. The total training epochs for Synapse are 30, for ACDC are 150, and for binary segmentation are 300. The batch size is 24 for Synapse and ACDC, and 8 for

Table 3. Comparison results on Synapse dataset. The evaluation metrics are HD95 (mm) and DSC in (%). DSC are reported for individual organs.  $\uparrow\downarrow$  denotes the higher (lower) the better.  $-$  means missing data from the source. **Bold** and underline represent the best and the second best results. The following text will continue to use these symbols to represent.

Methods	Average		Aotra	Gallbladder	Kidney (Left)	Kidney (Right)	Liver	Pancreas	Spleen	Stomach
	HD95 $\downarrow$	DSC $\uparrow$								
U-Net [46]	39.70	76.85	89.07	69.72	77.77	68.60	93.43	53.98	86.67	75.58
R50 U-Net [20, 46]	36.87	74.68	87.74	63.66	80.60	78.19	93.74	56.90	85.87	74.16
R50 Att-UNet [20, 40]	36.97	75.57	55.92	63.91	79.20	72.71	93.56	49.37	87.19	74.95
ViT [15] + CUP [9]	36.11	67.86	70.19	45.10	74.70	67.40	91.32	42.00	81.75	70.44
R50-ViT [15, 20] + CUP [9]	32.87	71.29	73.73	55.13	75.80	72.20	91.51	45.99	81.99	73.95
TransUNet [9]	31.69	77.48	87.23	63.16	81.87	77.02	94.08	55.86	85.08	75.62
SwinUNet [6]	21.55	79.13	85.47	66.53	83.28	79.61	94.29	56.58	90.66	76.60
TransClaw U-Net [7]	26.38	78.09	85.87	61.38	84.83	79.36	94.28	57.65	87.74	73.55
MT-UNet [53]	26.59	78.59	87.92	64.99	81.47	77.29	93.06	59.46	87.75	76.81
UCTransNet [52]	26.75	78.23	-	-	-	-	-	-	-	-
MISSFormer [23]	18.20	81.96	86.99	68.65	85.21	82.00	94.41	65.67	91.92	80.81
CASTFormer [57]	22.73	82.55	89.05	67.48	86.05	82.17	95.61	67.49	91.00	81.55
TransDeepLab [2]	21.25	80.16	86.04	69.16	84.08	79.88	93.53	61.19	89.00	78.40
LeViT-UNet-384 [55]	16.84	78.53	87.33	62.23	84.61	80.25	93.11	59.07	88.86	72.76
CTC-Net [58]	-	78.41	86.46	63.53	83.71	80.79	93.78	59.73	86.87	72.39
MS-UNet [8]	18.97	80.44	85.80	69.40	85.86	81.66	94.24	57.66	90.53	78.33
HiFormer-L [21]	19.14	80.69	87.03	68.61	84.23	78.37	94.07	60.77	90.44	82.03
PVT-CASCADE [44]	20.23	81.06	83.01	70.59	82.23	80.37	94.08	64.43	90.10	83.69
TransCASCADE [44]	17.34	82.68	86.63	68.48	<u>87.66</u>	<b>84.56</b>	94.43	65.33	90.79	83.52
AiA-UNet [43]	-	82.88	87.77	<b>74.33</b>	84.16	82.39	94.98	65.65	<b>92.77</b>	80.99
MetaSeg-B [26]	-	82.78	-	-	-	-	-	-	-	-
VM-UNet [47]	19.21	81.08	86.40	69.41	86.16	82.76	94.17	58.80	89.51	81.40
PVT-EMCAD-B2 [45]	<b>15.68</b>	<u>83.63</u>	88.14	68.87	<b>88.08</b>	<u>84.10</u>	95.26	68.51	<u>92.17</u>	<u>83.92</u>
SelfReg-UNet [46, 63]	-	80.34	88.74	<u>71.78</u>	85.32	80.71	93.80	62.22	84.78	75.39
SelfReg-SwinUnet [6, 63]	-	80.54	86.07	69.65	85.12	82.58	94.18	61.08	87.42	78.22
RWKV-UNet-T (ours)	17.83	81.58	89.28	64.18	86.03	83.76	95.09	63.50	90.36	80.44
RWKV-UNet-S (ours)	21.16	82.20	<u>89.36</u>	67.60	84.11	79.26	<b>95.60</b>	<u>68.86</u>	91.58	81.21
RWKV-UNet (ours)	<u>15.70</u>	<b>84.02</b>	<b>89.53</b>	68.94	87.63	84.07	<u>95.57</u>	<b>69.38</b>	90.95	<b>86.09</b>

Table 4. Comparison results on ACDC dataset. The evaluation metric is DSC in (%).

Methods	Average	RV	Myo	LV
R50 U-Net [20, 46]	87.55	87.10	80.63	94.92
ViT [15] + CUP [9]	81.45	81.46	70.71	92.18
R50-ViT [15, 20] + CUP [9]	87.57	86.07	81.88	94.75
R50 Att-UNet [20, 40]	86.75	87.58	79.20	93.47
TransUNet [9]	89.71	88.86	84.54	95.73
SwinUNet [6]	90.00	88.55	85.62	95.83
MT-UNet [53]	90.43	86.64	89.04	95.62
MS-UNet [8]	87.74	85.31	84.09	93.82
MISSFormer [23]	90.86	89.55	88.04	94.99
CTC-Net [58]	90.77	90.09	85.52	<u>96.72</u>
LeViT-UNet-384s [55]	90.32	89.55	87.64	93.76
PVT-CASCADE [44]	90.45	87.20	88.96	95.19
TransCASCADE [44]	91.63	89.14	<b>90.25</b>	95.50
PVT-EMCAD-B2 [45]	<u>92.12</u>	<u>90.65</u>	<u>89.68</u>	96.02
SelfReg-UNet [46, 63]	91.43	88.92	89.49	95.88
SelfReg-SwinUnet [6, 63]	91.49	89.49	89.27	95.70
RWKV-UNet-T (ours)	90.92	89.73	87.18	95.85
RWKV-UNet-S (ours)	91.64	89.77	88.48	96.65
RWKV-UNet (ours)	<b>92.17</b>	<b>90.86</b>	88.72	<b>96.92</b>

binary segmentation tasks. The initial learning rate is  $1e-3$  for Synapse,  $5e-4$  for ACDC, and  $1e-4$  for binary segmentation experiments. The minimum learning rates for

Synapse and ACDC are 0 and for binary segmentation are  $1e-5$ . The AdamW [36] optimizer and CosineAnnealingLR [37] scheduler are used. Test-time augmentation is used for Synapse and ACDC. The baseline results on binary segmentation tasks are run by ourselves. The loss function used is a mixed loss combining cross entropy (CE) loss and dice loss [39]:

$$\mathcal{L} = \alpha CE(\hat{y}, y) + \beta Dice(\hat{y}, y), \quad (12)$$

where  $\alpha$  and  $\beta$  are 0.5 and 0.5 for Synapse, 0.3 and 0.7 for ACDC, 0.5 and 1 for binary segmentation. Experiments for PVT-CASCADE [44] and PVT-EMCAD-B2 [45] use deep supervision strategy [29].

## 4.2. Comparison with State-of-the-arts

**Multi-organ Segmentation.** Table 3 shows that RWKV-UNet excels in abdomen organ segmentation on the Synapse multi-organ dataset, achieving the highest average DICE score of 84.02% and surpassing all SOTA CNN- and transformer-based methods. It also achieves 15.70 in HD95, only slightly lower than PVT-EMCAD-B2, demonstrating a strong ability to localize the organ boundary. Its performance on the most challenging task, pancreas segmentation, is the best, indicating its effectiveness in handling sample imbalance issues. Smaller models, RWKV-UNet-T and RWKV-UNet-S, also achieve remarkable results.

Table 5. Comparison results on BUSI, CVC-ClinicDB, CVC-ColonDB, Kvasir-SEG, ISIC 2017 and GLAS datasets. The evaluation metric are DSC in (%). Results with error bars are averaged over three runs with three different splits.

Methods	BUSI	CVC-ClinicDB	CVC-ColonDB	Kvasir-SEG	ISIC 2017	GLAS	Params.	FLOPs
U-Net [46]	74.90±1.15	89.22±4.07	83.43±5.24	84.94±2.60	82.94	88.56±0.63	7.8M	12.15G
Att-UNet [40]	78.14±1.25	90.86±4.09	84.75±6.55	86.21±2.15	83.96	89.14±0.54	8.7M	16.79G
UNet++ [61]	75.74±1.70	90.07±5.09	84.75±3.99	85.86±1.52	82.27	88.93±0.67	9.2M	34.77G
TransUNet [9]	79.35±2.45	93.91±2.28	90.72±3.92	91.34±0.01	86.09	91.58±0.15	0.1G	38.54G
FCBFormer [48]	80.66±0.28	91.15±3.50	85.23±5.21	91.09±0.96	84.56	91.13±0.25	53.0M	41.60G
PVT-CASCADE [44]	78.30±3.17	93.45±1.67	90.97±2.11	91.40±1.29	84.77	91.85±0.39	35.3M	8.40G
Rolling-UNet-M [31]	77.49±2.42	91.91±2.56	85.20±5.85	87.41±1.78	84.42	88.12±0.66	7.1M	8.31G
PVT-EMCAD-B2 [45]	79.22±1.07	93.39±1.64	91.27±1.84	90.37±1.10	84.05	91.77±0.09	26.8M	5.85G
U-KAN [30]	76.95±1.67	89.88±3.21	84.66±5.33	85.78±1.68	83.46	87.42±0.28	25.4M	10.59G
RWKV-UNet-T (ours)	79.47±1.35	95.05±0.67	89.56±5.26	91.26±2.13	85.59	91.96±0.31	3.3M	3.78G
RWKV-UNet-S (ours)	80.92±1.74	<b>95.58±0.69</b>	91.30±3.21	<b>91.78±1.24</b>	<b>86.38</b>	92.11±0.16	9.9M	7.75G
RWKV-UNet (ours)	<b>81.92±0.82</b>	95.26±0.70	<b>92.27±2.48</b>	91.26±1.27	85.32	<b>92.35±0.07</b>	17.4M	14.64G

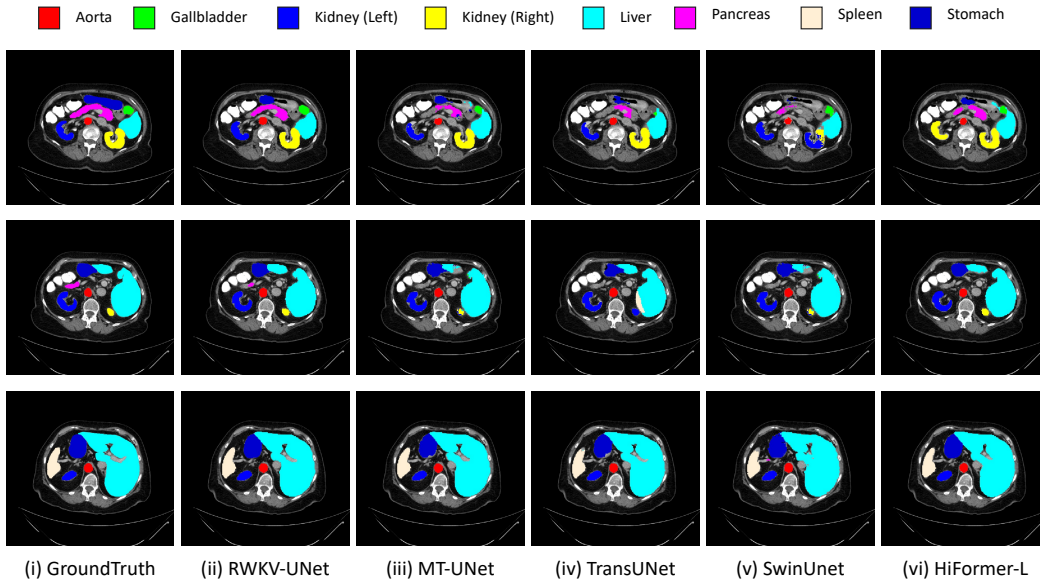


Figure 4. A qualitative comparison with previous SOTA methods on the Synapse dataset. The visual results demonstrate that our method achieves more accurate segmentation, especially in difficult tasks like pancreas segmentation.

**Cardiac Segmentation.** Table 4 shows that our model outperforms all SOTA models in the ACDC MRI cardiac segmentation task, achieving the best results in both RV and LV categories. The smaller models, RWKV-UNet-T and RWKV-UNet-S, also perform well.

**Binary Segmentation.** Table 5 shows that RWKV-UNet series show remarkable performance in the tasks of breast lesion, poly, skin lesion and grand segmentation, with much smaller parameters and computation load than TransUNet and FCBFormer. Meanwhile, it is observed that in some datasets the smaller model RWKV-UNet-S perform better.

### 4.3. Ablation and Analysis

**Effect of Pre-training for Encoder.** Whether to use pre-trained weights of RWKV-UNet encoder results in Table 6.

Table 6. Comparison results on Synapse dataset of whether to use pre-trained weights on ImageNet-1k or not.

Pre-training	Training Epochs	Average	
		HD95 ↓	DSC ↑
w/o	30	<b>13.94</b>	76.49
w/o	60	<u>14.03</u>	78.68
w/	30	15.70	<b>84.02</b>

Experimental results indicate that pre-training is essential because it significantly improves feature extraction by enabling the encoder to capture intricate patterns and hierarchical information. Notably, without pre-training, HD95 is higher. But DSC is a more important metric, providing a reliable assessment of segmentation quality directly, while HD95 can be overly sensitive to outliers.

Table 7. Comparison results of different decoder designs for RWKV-UNet on Synapse dataset.  $c \rightarrow c \rightarrow d$  denotes  $\text{Conv}_{1 \times 1} \rightarrow \text{Conv}_{1 \times 1} \rightarrow \text{DW-Conv}$  and  $c \rightarrow d \rightarrow c$  denotes  $\text{Conv}_{1 \times 1} \rightarrow \text{DW-Conv} \rightarrow \text{Conv}_{1 \times 1}$ .

Decoder	Kernel Size	Average		Flops
		HD95 ↓	DSC ↑	
Conv + upsample	3	24.95	81.77	11.38G
	3	23.44	82.10	11.06G
$c \rightarrow c \rightarrow d$ + upsample	5	25.53	81.84	11.07G
	7	20.78	81.57	11.08G
	9	<u>18.07</u>	<u>83.76</u>	11.10G
$c \rightarrow d \rightarrow c$ + upsample	3	21.68	83.33	11.08G
	5	22.26	83.74	11.11G
	7	22.90	82.54	11.16G
	9	<b>15.70</b>	<b>84.02</b>	11.22G

**Decoder Design.** In Tabel 7, we examine various sizes of convolution kernels, finding that the use of large kernels, such as  $9 \times 9$ , in the decoder significantly enhances the segmentation performance. This improvement is likely due to larger kernels capturing broader contextual information and preserving more spatial details, which enhances segmentation accuracy in medical images. We also compare different ways to construct the decoder block and the results show that  $\text{Conv}_{1 \times 1} \rightarrow \text{Conv}_{1 \times 1} \rightarrow \text{DW-Conv}$  performs better than  $\text{Conv}_{1 \times 1} \rightarrow \text{DW-Conv} \rightarrow \text{Conv}_{1 \times 1}$  and the common convolution layer, showing that DW-Conv operating on larger dimensions will help the decoding process.

**Channel Mix.** In VRWKV [16], a Channel Mix module is used after the Spatial Mix. In RWKV-UNet’s encoder, IR-RWKV blocks are designed without using Channel Mix as the pointwise convolution in the output layer performs both channel mix and feed-forward operations. We compare the results on the Synapse dataset with and without applying channel mix after spatial mix. All experiments are performed without pre-training, with a total of 60 epochs. The results are shown in Table 8, demonstrating that the channel mix is not essential for maintaining performance.

Table 8. Comparison of results on the Synapse dataset: effect of applying Channel Mix after Spatial Mix in the IR-RWKV blocks

Channel Mix	Average		FLOPs
	HD95 ↓	DSC ↑	
w/	15.29	<b>78.76</b>	19.49G
w/o (ours)	<b>14.03</b>	78.68	11.22G

**Skip Connections.** Comparison results of different skip connection designs for RWKV-UNet on the Synapse dataset are shown in Table 9. Experiments analyze variations in the number of skip connections and the inclusion of the CCM block. We prioritize retaining shallow skip connections because shallow layers tend to experience greater informa-

Table 9. Comparison results on different skip connections design of RWKV-UNet on Synapse dataset. Experiments are conducted on the number of skips and whether or not to use the CCM block.

Skips	CCM Block	Average		FLOPs
		HD95 ↓	DSC ↑	
0	w/o	23.39	74.19	9.25 G
1	w/o	17.17	79.76	9.41 G
1	w/	19.56	79.98	9.63 G
2	w/o	<u>16.08</u>	80.90	9.49 G
2	w/	19.97	81.11	10.24 G
3	w/o	22.72	<u>81.14</u>	9.56 G
3	w/	<b>15.70</b>	<b>84.02</b>	11.22 G

tion loss. The results show that, like other UNet’s variants, adequate skip connections are essential for RWKV-UNet’s performance. Furthermore, the results show that the CCM module can significantly improve the model segmentation results. Even if only one or two inputs from the encoder (when only one input, the CCM block degrades to a “channel mix bridge”), the CCM block can still lead to increments in DSC. Admittedly, the CCM module increases the computational load to some extent due to the aggregation of global information.

## 5. Conclusion

In this study, we introduce RWKV-UNet, a novel architecture that integrates the RWKV architecture with U-Net. By combining the strengths of convolutional networks for local feature extraction and RWKV’s ability to model global context, our model significantly improves medical image segmentation accuracy. The proposed enhancements, such as the IR-RWKV module and the CCM module, contribute to a more precise feature representation and information fusion across different scales. Experimental results on benchmark datasets demonstrate that RWKV-UNet surpasses all SOTA CNN- and transformer-based methods. Its variants (RWKV-UNet-S and RWKV-UNet-T) offer a practical balance between performance and computational efficiency. Our approach has a strong potential to advance medical image analysis, particularly in clinical settings where both accuracy and efficiency are paramount.

**Limitations and Future Work.** RWKV-UNet is a powerful 2D medical image segmentation model that effectively combines RWKV with convolution, but it is currently not applicable to 3D imaging. In the future, we plan to extend the model to 3D for handling volume data and to explore the potential of RWKV-based foundational models for medical imaging. We also aim to develop ultra-lightweight RWKV-based models tailored for ‘bed-side healthcare’ applications, preserving segmentation accuracy while enhancing adaptability and speed further.

## References

- [1] Walid Al-Dhabyani, Mohammed Gomaa, Hussien Khaled, and Aly Fahmy. Dataset of breast ultrasound images. *Data in brief*, 28:104863, 2020. 2, 5, 12
- [2] Reza Azad, Moein Heidari, Moein Shariatnia, Ehsan Khodapanah Aghdam, Sanaz Karimijafarbigloo, Ehsan Adeli, and Dorit Merhof. Transdeeplab: Convolution-free transformer-based deeplab v3+ for medical image segmentation. In *International Workshop on PRedictive Intelligence In MEdicine*, pages 91–102. Springer, 2022. 2, 5, 6
- [3] Jorge Bernal, Javier Sánchez, and Fernando Vilarino. Towards automatic polyp detection with a polyp appearance model. *Pattern Recognition*, 45(9):3166–3182, 2012. 2, 5, 12
- [4] Jorge Bernal, F Javier Sánchez, Gloria Fernández-Esparrach, Debora Gil, Cristina Rodríguez, and Fernando Vilariño. Wm-dova maps for accurate polyp highlighting in colonoscopy: Validation vs. saliency maps from physicians. *Computerized medical imaging and graphics*, 43:99–111, 2015. 2, 5, 12
- [5] Olivier Bernard, Alain Lalande, Clement Zotti, Frederick Cervenansky, Xin Yang, Pheng-Ann Heng, Irem Cetin, Karim Lekadir, Oscar Camara, Miguel Angel Gonzalez Ballester, et al. Deep learning techniques for automatic mri cardiac multi-structures segmentation and diagnosis: is the problem solved? *IEEE transactions on medical imaging*, 37(11):2514–2525, 2018. 2, 5, 12
- [6] Hu Cao, Yueyue Wang, Joy Chen, Dongsheng Jiang, Xiaopeng Zhang, Qi Tian, and Manning Wang. Swin-unet: Unet-like pure transformer for medical image segmentation. In *European conference on computer vision*, pages 205–218. Springer, 2022. 5, 6
- [7] Yao Chang, Hu Menghan, Zhai Guangtao, and Zhang Xiao-Ping. Transclaw u-net: Claw u-net with transformers for medical image segmentation. *arXiv preprint arXiv:2107.05188*, 2021. 2, 5, 6
- [8] Haoyuan Chen, Yufei Han, Yanyi Li, Pin Xu, Kuan Li, and Jianping Yin. Ms-unet: Swin transformer u-net with multi-scale nested decoder for medical image segmentation with small training data. In *Chinese Conference on Pattern Recognition and Computer Vision (PRCV)*, pages 472–483. Springer, 2023. 2, 5, 6
- [9] Jieneng Chen, Yongyi Lu, Qihang Yu, Xiangde Luo, Ehsan Adeli, Yan Wang, Le Lu, Alan L Yuille, and Yuyin Zhou. Transunet: Transformers make strong encoders for medical image segmentation. *arXiv preprint arXiv:2102.04306*, 2021. 1, 2, 5, 6, 7, 12, 13
- [10] Jieneng Chen, Jieru Mei, Xianhang Li, Yongyi Lu, Qihang Yu, Qingyue Wei, Xiangde Luo, Yutong Xie, Ehsan Adeli, Yan Wang, et al. 3d transunet: Advancing medical image segmentation through vision transformers. *arXiv preprint arXiv:2310.07781*, 2023. 12, 13
- [11] Liang-Chieh Chen, Yukun Zhu, George Papandreou, Florian Schroff, and Hartwig Adam. Encoder-decoder with atrous separable convolution for semantic image segmentation. In *Proceedings of the European conference on computer vision (ECCV)*, pages 801–818, 2018. 13
- [12] Özgün Çiçek, Ahmed Abdulkadir, Soeren S Lienkamp, Thomas Brox, and Olaf Ronneberger. 3d u-net: learning dense volumetric segmentation from sparse annotation. In *Medical Image Computing and Computer-Assisted Intervention—MICCAI 2016: 19th International Conference, Athens, Greece, October 17–21, 2016, Proceedings, Part II 19*, pages 424–432. Springer, 2016. 2
- [13] Noel CF Codella et al. Skin lesion analysis toward melanoma detection: A challenge at the 2017 international symposium on biomedical imaging (isbi), hosted by the international skin imaging collaboration (isic). In *2018 IEEE 15th international symposium on biomedical imaging (ISBI 2018)*, pages 168–172. IEEE, 2018. 2, 5, 12
- [14] Jia Deng, Wei Dong, Richard Socher, Li-Jia Li, Kai Li, and Li Fei-Fei. Imagenet: A large-scale hierarchical image database. In *2009 IEEE conference on computer vision and pattern recognition*, pages 248–255. Ieee, 2009. 4
- [15] Alexey Dosovitskiy. An image is worth 16x16 words: Transformers for image recognition at scale. *arXiv preprint arXiv:2010.11929*, 2020. 5, 6
- [16] Yuchen Duan, Weiyun Wang, Zhe Chen, Xizhou Zhu, Lewei Lu, Tong Lu, Yu Qiao, Hongsheng Li, Jifeng Dai, and Wenhai Wang. Vision-rwkv: Efficient and scalable visual perception with rwkv-like architectures. *arXiv preprint arXiv:2403.02308*, 2024. 1, 2, 8
- [17] Albert Gu and Tri Dao. Mamba: Linear-time sequence modeling with selective state spaces. *arXiv preprint arXiv:2312.00752*, 2023. 1, 2
- [18] Dongchen Han, Xuran Pan, Yizeng Han, Shiji Song, and Gao Huang. Flatten transformer: Vision transformer using focused linear attention. In *Proceedings of the IEEE/CVF international conference on computer vision*, pages 5961–5971, 2023. 4
- [19] Ali Hatamizadeh, Vishwesh Nath, Yucheng Tang, Dong Yang, Holger R Roth, and Daguang Xu. Swin unetr: Swin transformers for semantic segmentation of brain tumors in mri images. In *International MICCAI brainlesion workshop*, pages 272–284. Springer, 2021. 2
- [20] Kaiming He, Xiangyu Zhang, Shaoqing Ren, and Jian Sun. Deep residual learning for image recognition. In *Proceedings of the IEEE conference on computer vision and pattern recognition*, pages 770–778, 2016. 5, 6
- [21] Moein Heidari, Amirhossein Kazerouni, Milad Soltany, Reza Azad, Ehsan Khodapanah Aghdam, Julien Cohen-Adad, and Dorit Merhof. Hiformer: Hierarchical multi-scale representations using transformers for medical image segmentation. In *Proceedings of the IEEE/CVF winter conference on applications of computer vision*, pages 6202–6212, 2023. 1, 2, 5, 6
- [22] Huimin Huang, Lanfen Lin, Ruofeng Tong, Hongjie Hu, Qiaowei Zhang, Yutaro Iwamoto, Xianhua Han, Yen-Wei Chen, and Jian Wu. Unet 3+: A full-scale connected unet for medical image segmentation. In *ICASSP 2020-2020 IEEE international conference on acoustics, speech and signal processing (ICASSP)*, pages 1055–1059. IEEE, 2020. 1, 2
- [23] Xiaohong Huang, Zhifang Deng, Dandan Li, Xueguang Yuan, and Ying Fu. Missformer: An effective transformer

- for 2d medical image segmentation. *IEEE Transactions on Medical Imaging*, 42(5):1484–1494, 2022. 2, 5, 6
- [24] Fabian Isensee, Paul F Jaeger, Simon AA Kohl, Jens Petersen, and Klaus H Maier-Hein. nnu-net: a self-configuring method for deep learning-based biomedical image segmentation. *Nature methods*, 18(2):203–211, 2021. 13
- [25] Debesh Jha et al. Kvasir-seg: A segmented polyp dataset. In *MultiMedia Modeling: 26th International Conference, MMM 2020, Daejeon, South Korea, January 5–8, 2020, Proceedings, Part II* 26, pages 451–462. Springer, 2020. 2, 5, 12
- [26] Beoungwoo Kang, Seunghun Moon, Yubin Cho, Hyunwoo Yu, and Suk-Ju Kang. Metaseg: Metaformer-based global contexts-aware network for efficient semantic segmentation. In *Proceedings of the IEEE/CVF Winter Conference on Applications of Computer Vision (WACV)*, pages 434–443, 2024. 2, 5, 6
- [27] Bennett Landman, Zhoubing Xu, J Igelsias, Martin Styner, Thomas Langerak, and Arno Klein. Miccai multi-atlas labeling beyond the cranial vault—workshop and challenge. In *Proc. MICCAI Multi-Atlas Labeling Beyond Cranial Vault—Workshop Challenge*, page 12, 2015. 2, 5, 12
- [28] Yann LeCun, Yoshua Bengio, and Geoffrey Hinton. Deep learning. *nature*, 521(7553):436–444, 2015. 1
- [29] Chen-Yu Lee, Saining Xie, Patrick Gallagher, Zhengyou Zhang, and Zhuowen Tu. Deeply-supervised nets. In *Artificial intelligence and statistics*, pages 562–570. Pmlr, 2015. 6
- [30] Chenxin Li, Xinyu Liu, Wuyang Li, Cheng Wang, Hengyu Liu, Yifan Liu, Zhen Chen, and Yixuan Yuan. U-kan makes strong backbone for medical image segmentation and generation, 2024. 2, 5, 7
- [31] Chenxin Li, Xinyu Liu, Wuyang Li, Cheng Wang, Hengyu Liu, and Yixuan Yuan. U-kan makes strong backbone for medical image segmentation and generation. *arXiv preprint arXiv:2406.02918*, 2024. 5, 7
- [32] Hanchao Li, Pengfei Xiong, Jie An, and Lingxue Wang. Pyramid attention network for semantic segmentation. *arXiv preprint arXiv:1805.10180*, 2018. 13
- [33] Weibin Liao, Yinghao Zhu, Xinyuan Wang, Chengwei Pan, Yasha Wang, and Liantao Ma. Lightm-unet: Mamba assists in lightweight unet for medical image segmentation. *arXiv preprint arXiv:2403.05246*, 2024. 1, 2
- [34] Jiarun Liu, Hao Yang, Hong-Yu Zhou, Yan Xi, Lequan Yu, Cheng Li, Yong Liang, Guangming Shi, Yizhou Yu, Shaoting Zhang, et al. Swin-umamba: Mamba-based unet with imagenet-based pretraining. In *International Conference on Medical Image Computing and Computer-Assisted Intervention*, pages 615–625. Springer, 2024. 2
- [35] Yutong Liu, Haijiang Zhu, Mengting Liu, Huaiyuan Yu, Zihan Chen, and Jie Gao. Rolling-unet: Revitalizing mlp’s ability to efficiently extract long-distance dependencies for medical image segmentation. In *Proceedings of the AAAI Conference on Artificial Intelligence*, pages 3819–3827, 2024. 2
- [36] I Loshchilov. Decoupled weight decay regularization. *arXiv preprint arXiv:1711.05101*, 2017. 4, 6
- [37] Ilya Loshchilov and Frank Hutter. Sgdr: Stochastic gradient descent with warm restarts. *arXiv preprint arXiv:1608.03983*, 2016. 6
- [38] Jun Ma, Feifei Li, and Bo Wang. U-mamba: Enhancing long-range dependency for biomedical image segmentation. *arXiv preprint arXiv:2401.04722*, 2024. 1, 2
- [39] Fausto Milletari, Nassir Navab, and Seyed-Ahmad Ahmadi. V-net: Fully convolutional neural networks for volumetric medical image segmentation. In *2016 fourth international conference on 3D vision (3DV)*, pages 565–571. Ieee, 2016. 2, 6
- [40] Ozan Oktay, Jo Schlemper, Loic Le Folgoc, Matthew Lee, Mattias Heinrich, Kazunari Misawa, Kensaku Mori, Steven McDonagh, Nils Y Hammerla, Bernhard Kainz, et al. Attention u-net: Learning where to look for the pancreas. *arXiv preprint arXiv:1804.03999*, 2018. 1, 2, 5, 6, 7, 13
- [41] Bo Peng, Eric Alcaide, Quentin Anthony, Alon Albalak, Samuel Arcadinho, Stella Biderman, Huanqi Cao, Xin Cheng, Michael Chung, Leon Derczynski, et al. Rwkv: Reinventing rnns for the transformer era. In *Findings of the Association for Computational Linguistics: EMNLP 2023*, pages 14048–14077, 2023. 1, 2
- [42] Ledan Qian, Caiyun Wen, Yi Li, Zhongyi Hu, Xiao Zhou, Xiaonyu Xia, and Soo-Hyung Kim. Multi-scale context unet-like network with redesigned skip connections for medical image segmentation. *Computer Methods and Programs in Biomedicine*, 243:107885, 2024. 2
- [43] Jianfeng Qin, Xinwei He, Jiakun Yu, Wen Zhang, Jinhai Xiang, and Lulu Wu. Aia-unet: Attention in attention for medical image segmentation. In *2023 IEEE International Conference on Bioinformatics and Biomedicine (BIBM)*, pages 2179–2182. IEEE, 2023. 5, 6
- [44] Md Mostafijur Rahman and Radu Marculescu. Medical image segmentation via cascaded attention decoding. In *Proceedings of the IEEE/CVF Winter Conference on Applications of Computer Vision*, pages 6222–6231, 2023. 5, 6, 7
- [45] Md Mostafijur Rahman, Mustafa Munir, and Radu Marculescu. Emcad: Efficient multi-scale convolutional attention decoding for medical image segmentation. In *Proceedings of the IEEE/CVF Conference on Computer Vision and Pattern Recognition*, pages 11769–11779, 2024. 5, 6, 7
- [46] Olaf Ronneberger, Philipp Fischer, and Thomas Brox. U-net: Convolutional networks for biomedical image segmentation. In *Medical image computing and computer-assisted intervention—MICCAI 2015: 18th international conference, Munich, Germany, October 5-9, 2015, proceedings, part III 18*, pages 234–241. Springer, 2015. 1, 5, 6, 7, 13
- [47] Jiacheng Ruan and Suncheng Xiang. Vm-unet: Vision mamba unet for medical image segmentation. *arXiv preprint arXiv:2402.02491*, 2024. 1, 2, 4, 5, 6
- [48] Edward Sanderson and Bogdan J Matuszewski. Fcn-transformer feature fusion for polyp segmentation. In *Annual Conference on Medical Image Understanding and Analysis*, pages 892–907. Springer, 2022. 5, 7
- [49] Korsuk Sirinukunwattana, Josien PW Pluim, Hao Chen, Xiaojuan Qi, Pheng-Ann Heng, Yun Bo Guo, Li Yang Wang, Bogdan J Matuszewski, Elia Bruni, Urko Sanchez, et al.

- Gland segmentation in colon histology images: The glas challenge contest. *Medical image analysis*, 35:489–502, 2017. [2](#), [5](#), [12](#)
- [50] Jeya Maria Jose Valanarasu and Vishal M Patel. Unext: Mlp-based rapid medical image segmentation network. In *International conference on medical image computing and computer-assisted intervention*, pages 23–33. Springer, 2022. [2](#), [12](#)
- [51] A Vaswani. Attention is all you need. *Advances in Neural Information Processing Systems*, 2017. [4](#)
- [52] Haonan Wang, Peng Cao, Jiaqi Wang, and Osmar R Zaiane. Utransnet: rethinking the skip connections in u-net from a channel-wise perspective with transformer. In *Proceedings of the AAAI conference on artificial intelligence*, pages 2441–2449, 2022. [2](#), [5](#), [6](#)
- [53] Hongyi Wang, Shiao Xie, Lanfen Lin, Yutaro Iwamoto, Xian-Hua Han, Yen-Wei Chen, and Ruofeng Tong. Mixed transformer u-net for medical image segmentation. In *ICASSP 2022-2022 IEEE international conference on acoustics, speech and signal processing (ICASSP)*, pages 2390–2394. IEEE, 2022. [1](#), [2](#), [5](#), [6](#)
- [54] Ziyang Wang, Jian-Qing Zheng, Yichi Zhang, Ge Cui, and Lei Li. Mamba-unet: Unet-like pure visual mamba for medical image segmentation. *arXiv preprint arXiv:2402.05079*, 2024. [2](#)
- [55] Guoping Xu, Xuan Zhang, Xinwei He, and Xinglong Wu. Levit-unet: Make faster encoders with transformer for medical image segmentation. In *Chinese Conference on Pattern Recognition and Computer Vision (PRCV)*, pages 42–53. Springer, 2023. [2](#), [5](#), [6](#)
- [56] Zhiwen Yang, Hui Zhang, Dan Zhao, Bingzheng Wei, and Yan Xu. Restore-rwkv: Efficient and effective medical image restoration with rwkv, 2024. [2](#)
- [57] Chenyu You, Ruihan Zhao, Fenglin Liu, Siyuan Dong, Sandeep Chinchali, Ufuk Topcu, Lawrence Staib, and James Duncan. Class-aware adversarial transformers for medical image segmentation. *Advances in Neural Information Processing Systems*, 35:29582–29596, 2022. [2](#), [5](#), [6](#)
- [58] Feiniu Yuan, Zhengxiao Zhang, and Zhijun Fang. An effective cnn and transformer complementary network for medical image segmentation. *Pattern Recognition*, 136:109228, 2023. [5](#), [6](#)
- [59] Zhengxin Zhang, Qingjie Liu, and Yunhong Wang. Road extraction by deep residual u-net. *IEEE Geoscience and Remote Sensing Letters*, 15(5):749–753, 2018. [2](#)
- [60] Xudong Zhou and Tianxiang Chen. Bsbp-rwkv: Background suppression with boundary preservation for efficient medical image segmentation. In *ACM Multimedia 2024*, 2024. [2](#)
- [61] Zongwei Zhou, Md Mahfuzur Rahman Siddiquee, Nima Tajbakhsh, and Jianming Liang. Unet++: A nested u-net architecture for medical image segmentation. In *Deep Learning in Medical Image Analysis and Multimodal Learning for Clinical Decision Support: 4th International Workshop, DLMIA 2018, and 8th International Workshop, ML-CDS 2018, Held in Conjunction with MICCAI 2018, Granada, Spain, September 20, 2018, Proceedings 4*, pages 3–11. Springer, 2018. [1](#), [2](#), [7](#), [13](#)
- [62] Lianghui Zhu, Bencheng Liao, Qian Zhang, Xinlong Wang, Wenyu Liu, and Xinggang Wang. Vision mamba: Efficient visual representation learning with bidirectional state space model. *arXiv preprint arXiv:2401.09417*, 2024. [1](#), [2](#), [4](#)
- [63] Wenhui Zhu, Xiwen Chen, Peijie Qiu, Mohammad Farazi, Aristeidis Sotiras, Abolfazl Razi, and Yalin Wang. Selfreg-unet: Self-regularized unet for medical image segmentation, 2024. [5](#), [6](#)
- [64] Nikolaos Zioulis, Georgios Albanis, Petros Drakoulis, Federico Alvarez, Dimitrios Zarpalas, and Petros Daras. Hybrid skip: A biologically inspired skip connection for the unet architecture. *IEEE Access*, 10:53928–53939, 2022. [2](#)

## Appendix

The supplementary material gives more specific details of our experimental settings, and presents more comprehensive analysis and results of our RWKV-UNet to facilitate the comparison of subsequent methods:

- **Sec. A** provides introduction to datasets and corresponding splitting settings used in this paper.
- **Sec. B.1** provides comparison results on Synapse dataset to explore the effect of applying DW-Conv after Spatial Mix in IR-RWKV blocks.
- **Sec. B.2** provides comparison results of different methods on Synapse dataset with larger inputs.

### A. Introduction to datasets

1) The Synapse multi-organ segmentation dataset [27]: 30 abdominal CT scans from the MICCAI 2015 Multi-Atlas Abdomen Labeling Challenge are used. The dataset is split into 18 training cases and 12 cases for validation following the setting in [9].

2) The Automated Cardiac Diagnosis Challenge (ACDC) [5]: This dataset gathers examinations obtained by MRI scanners. Each patient scan is manually annotated with ground truth data for the left ventricle (LV), right ventricle (RV), and myocardium (MYO). The dataset is split into 70 training cases, along with 10 cases for validation and 20 for testing following the setting in [9].

3) Breast Ultrasound Images Dataset (BUSI) [1]: This dataset contains breast ultrasound images collected from women between 25 and 75 years old. The dataset consists of 780 pairs of images in normal, benign, and malignant, with corresponding masks. Unlike the setting in [50], we include all three classes in the dataset. The dataset is split into the training set, the validation set and the validation set with a ratio of 8:1:1 with three different random states.

4) CVC-ClinicDB [4]: This dataset contains frames extracted from colonoscopy videos that contain several examples of polyps. The dataset consists of 612 pairs of images and corresponding masks. The dataset is split into the training set, the validation set and the testing set with a ratio of 8:1:1 with three different random states.

5) CVC-ColonDB [3]: This dataset includes 380 images, each with a resolution of  $574 \times 500$  pixels. These images were selected from a pool of 12,000 images obtained from 15 short colonoscopy videos, with only these 380 images being annotated. The dataset is split into the training set, the validation set and the testing set with a ratio of 8:1:1 with three different random states.

6) Kvasir-SEG [25]: This dataset comprises 1000 polyp images and their corresponding ground truth masks with resolutions ranging from  $332 \times 487$  to  $1920 \times 1072$  pixels. The dataset is split into the training set, the validation set and the testing set with a ratio of 8:1:1 with three different ran-

dom states.

7) ISIC 2017 [13]: This dataset contains skin lesions images for Skin Lesion Analysis toward Melanoma Detection Challenge at the International Symposium on Biomedical Imaging (ISBI) 2017. There are 2000 pairs of images and corresponding masks in the training set, 150 pairs in the validation set, and 600 pairs in the testing set.

8) GlaS [49]: This dataset is designed for gland segmentation. It consists of 165 whole-slide images (WSIs), with 85 images designated for training and 80 for testing. The training dataset is split into a new training set and a validation set with a ratio of 9:1 with three different random states.

### B. More Ablation and Exploration Analysis

#### B.1. Depth-wise Convolution in IR-RWKV Blocks

The comparison results to explore the effect of DW-Conv after Spatial Mix in IR-RWKV blocks are shown in Table A1. The inclusion of DW-Conv demonstrates a notable improvement in performance metrics. The slight increase in computational cost is minimal and well-justified given the significant gains in performance. This indicates that in IR-RWKV blocks, DW-Conv plays a critical role. It provides local information that complements the long-range dependencies captured by Spatial Mix, effectively enhancing model accuracy. Without pre-training, relying solely on Spatial Mix without the inclusion of local information from DW-Conv limits the model’s ability to fully capture fine-grained spatial details. This demonstrates the necessity of integrating both components to achieve a balanced representation of local and global features.

Table A1. Comparison of results on the Synapse dataset: effect of applying DW-Conv after Spatial Mix in IR-RWKV blocks

DW-Conv	Average		FLOPs
	HD95 ↓	DSC ↑	
w/o	16.55	75.56	11.14G
w/ (ours)	<b>14.03</b>	<b>78.68</b>	11.22G

#### B.2. Larger Resolution Inputs

The comparison results of different methods with  $512 \times 512$  input in the Synapse dataset are shown in Table A2. The average Dice scores of other methods are from [10]. Our results indicate that when the input resolution is increased to  $512 \times 512$ , our model demonstrates an improvement in performance. Although the improvement is not significant, it still maintains the best performance overall. Furthermore, compared to TransUNet, the computational overhead associated with the resolution increase is less severe, showcasing the efficiency of our model at higher resolutions.

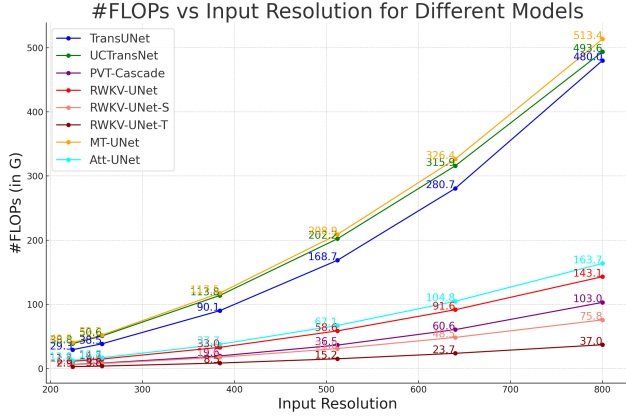


Figure A1. #FLOPs vs input resolutions. for different methods. The input channel is 1 and the output is 9 (aligned with settings on Synapse dataset).

Table A2. Comparison of different methods with  $512 \times 512$  resolution input on the Synapse dataset. The evaluation metric are DSC in (%). The average DSC of other methods are from [10].

Method	Average	FLOPs
U-Net [46]	81.34	-
Pyramid Attention [32]	80.08	-
DeepLabv3+ [11]	82.50	-
UNet++ [61]	81.60	-
Attention U-Net [40]	80.88	-
nnU-Net [24]	82.92	-
TransUNet [9]	84.36	168.7G
RWKV-UNet (ours) [9]	<b>85.52</b>	58.6G

As shown in Figure A1, the RWKV-UNet series demonstrates advantages in handling high-resolution inputs, as shown in the FLOPs comparison. Particularly for larger resolutions, the RWKV-UNet models maintain significantly lower computational costs compared to other high-performance architectures like transUNet and MT-UNet. It demonstrates that linear attention outperforms traditional Transformers in efficiency, enabling faster and more memory-efficient processing of high-resolution inputs and long sequences.